Advances in Applied Mathematics and Mechanics
Adv. Appl. Math. Mech., Vol. **8**, No. 4, pp. 616-647

DOI: 10.4208/aamm.2014.m829
August 2016

Numerical Simulations of Two Coaxial Vortex Rings Head-on Collision

Hui Guan[1], Zhi-Jun Wei[2], Elizabeth Rumenova Rasolkova[2] and Chui-Jie Wu[2,*]

[1] *College of Meteorology and Oceanography, PLA University of Science and Technology, Nanjing 211101, China*
[2] *State Key Laboratory of Structural Analysis for Industrial Equipment, School of Aeronautics and Astronautics, Dalian University of Technology, Dalian 116024, China*

Received 7 November 2014; Accepted (in revised version) 24 June 2015

Abstract. Vortex rings have been a subject of interest in vortex dynamics due to a plethora of physical phenomena revealed by their motions and interactions within a boundary. The present paper is devoted to physics of a head-on collision of two vortex rings in three dimensional space, simulated with a second order finite volume scheme and compressible. The scheme combines non-iterative approximate Riemann-solver and piecewise-parabolic reconstruction used in inviscid flux evaluation procedure. The computational results of vortex ring collisions capture several distinctive phenomena. In the early stages of the simulation, the rings propagate under their own self-induced motion. As the rings approach each other, their radii increase, followed by stretching and merging during the collision. Later, the two rings have merged into a single doughnut-shaped structure. This structure continues to extend in the radial direction, leaving a web of particles around the centers. At a later time, the formation of ringlets propagate radially away from the center of collision, and then the effects of instability involved leads to a reconnection in which small-scale ringlets are generated. In addition, it is shown that the scheme captures several experimentally observed features of the ring collisions, including a turbulent breakdown into small-scale structures and the generation of small-scale radially propagating vortex rings, due to the modification of the vorticity distribution, as a result of the entrainment of background vorticity and helicity by the vortex core, and their subsequent interaction.

AMS subject classifications: 65M10, 78A48

Key words: Three dimensional numerical simulation, vortex ring, collision, large eddy-simulation.

*Corresponding author.
Email: cjwudut@dlut.edu.cn (C. J. Wu)

 ©2016 Global Science Press

https://doi.org/10.4208/aamm.2014.m829 Published online by Cambridge University Press

1 Introduction

This article includes research into the regularities of formation and motion of one of the most interesting types of liquid and gas vortex motions–vortex ring. It is well known that a vortex ring deforms as it collides in an obstacle. A recent experiment devoted to a head-on collision of two vortex rings in three dimensional space [1] shows that the deformation of the rings is not so easy to study and predict. A question has been raised as how the collision would affect the motion of a vortex rings and the vorticity distribution. The present article is an attempt to address this issue. For the reader's convenience, this article is separated in four sections, each presenting a specific topic, each part containing a few sections.

The vortex flow is one of the fundamental types of fluid and gas motion. It is characterized by the localization of vorticity in bounded regions of a space, beyond which the vorticity is absent or rapidly falls to zero. Concentrated vortices are often observed in nature, exemplified through atmospheric cyclones, whirlwinds and tornados, oceanic vortices, whirlpools on a water surface, and ring vortices caused by explosive out burs of volcanoes. In technical devices, concentrated vortices are formed when the flow is separated from sharp edges of flying vehicles and ships, airplane wings, etc. One remarkable and frequent type of concentrated vortices is a vortex ring which constitutes of a vortex tube closed into a toroidal ring, moving in a surrounding fluid. It appears like an isolated body which is out of contact with solid boundaries of the flow region, if such boundaries exist. The formation and motion of vortex rings are an important part of the dynamics of a continuum medium and have been studied for more than a century. These investigations promoted elucidation of many general mechanisms of vortex motions, and recently provided a basis for developing high efficiency operating procedures [2].

Originally, vortex rings sparked interest because of simplicity of their generation and observation, and due to approximately steady characteristic of fluid motion relative to the vortex ring. Systematic scientific studies of vortex rings have been performed by many famous researchers in mechanics and physics, e.g., Helmholtz (1858); Kelvin (1867); Reynolds (1876); Thomson and Newall (1885); Prandtl and Tietjens (1934); Joukowski (1937); Lamb (1932); Prandtl (1949); Taylor (1953); Sommerfeld (1950); Feynman (1964); Kirchhoff (1962); Batchelor (1967). Their investigations resulted in the development of mathematical models for vortex rings in the framework of an ideal (inviscid) fluid, and formulas were obtained for determination of the fundamental vortex ring properties: impulse, energy, translational velocity, and streamline structure. For a long time the concepts of vortex rings were based only on these theoretical results.

Vortex rings have fascinated researchers for a long time because of their frequent appearance in nature and technology, as well as the way they can be easily produced experimentally. They are mainly generated by exhaustion of a finite-length submerged jet from a circular orifice or from an open end of a cylindrical tube. Using this technique, it is easy to determine and control the condition of vortex ring formation. Here the problem of obtaining accurate analytical estimations of the properties of the vortex ring being

https://doi.org/10.4208/aamm.2014.m829 Published online by Cambridge University Press

formed also emerges and depends on the parameters of the jet and experimental facility. This problem attracted the attention of many researchers, e.g., Wedemeier (1961); Bardotti and Bertotti (1964); Saffman (1970); Didden (1979); Pullin (1979); Vladimirov and Tarasov (1980); Shariff and Leonard (1992); Nitzsche (1996); Sullivan (2008). The review articles show the rich variety of research in vortex rings, encompassing analytical, numerical and experimental results.

In the present study, we are concerned with the problem of head-on collision of two coaxial vortex rings. In her visualization study, Oshima [3] observed that the smoke cross-sections of vortex rings deform from a circular to a head with a long trailing tail during the collision. Subsequently, the head pinches off from the tail and continually increases in radius. At larger radii, azimuthal waviness pinches to form a dozen smaller rings. Kambe and his coworkers [4, 5] studied head-on collision by numerical simulation, primarily to test theories of vortex sound generation. The author indicated that the viscous effect is important during collision. On the other hand, Shariff, using contour dynamics, revealed some of the inviscid effects of head-on collisions of vortex rings and suggested that inviscid core deformation was sufficient for acoustic emission. Recently, Lim and Nickels [1] used coloured dye to reveal the detailed structure of the small rings and several other features, including short-wavelength instability around the circumference of the colliding rings and a turbulent cloud with occasional appearance of small rings. Their experimental results indicate that the viscous effect plays a role during the process of inter action of the vortex rings.

Another experimental and numerical investigation of two coaxial vortex rings collision in three dimensions [6], point that the enstrophy, rather than circulation, revealed three stages of evolution of the vortex rings prior to their breakdown. These include the stages of free-travelling, vortex stretching and viscous dissipation dominance.

The original Lagrangian LES attempts may be traced to Chorin's hairpin removal algorithms [7,8]. Hairpin removal schemes have been used in various applications, including boundary layers [9], vortex breakdown [10], and vortex reconnection [11]. Recently proposed extensions of the hairpin removal scheme are based on renormalized equations of motion for large scales [12,13] including a scale-dependent "dielectric constant" which accounts for the missing scales in the Biot-Savart law [14]. Recent vortex rings collision numerical scheme in three dimensions [15], combines a 3D, adaptive, viscous, vortex element method with a dynamic eddy viscosity model of the sub-filter scale stresses. The sub-filter scale vorticity model consists of approximating the effect of unresolved vorticity stresses using a gradient-diffusion eddy viscosity model. The scheme captures several features including turbulent break down into small-scale structures and the generation of small-scale radially propagating vortex rings.

These studies, not only enable us to assess the range of validity assumed for the numerical simulation, but also provide us with a rational basis for further instability analysis. But unfortunately, the recent result did not provide quantitative data such as velocity and vorticity field. It is, therefore, unclear under which conditions and to what effect is significant for the behavior of the vortex ring during the collision. A satisfactory answer

https://doi.org/10.4208/aamm.2014.m829 Published online by Cambridge University Press

to this problem needs further experimental and numerical clarification.

Hence, a computational model has been adopted, described and applied to LES for colliding two coaxial vortex rings.

2 Second order explicit scheme (SOES)

This section is a brief description of 3D Cartesian-grid finite volume scheme [16] for compressible unsteady flow and its application to LES [17] of two simple test cases made by Chernousov [18]. The main features of this scheme are: (i) non-iterative approximate Riemann solver, based on linearized differential relations along characteristics of one dimensional hyperbolic conservation law; and (ii) piecewise parabolic construction used in inviscid fluxes evaluation procedure.

2.1 Mathematical model

The governing equations are filtered compressible Navier-Stokes equations. After Favre filtering, dropping nonlinear terms and assuming sub-grid turbulence behavior to be analogous to molecular dissipation mechanism, we obtain the following approximation to the filtered equations (in tensor notation):

$$\begin{cases} \dfrac{\partial \rho}{\partial t}+\dfrac{\partial}{\partial x_j}(\rho u_j)=0, \\ \dfrac{\partial \rho u_i}{\partial t}+\dfrac{\partial}{\partial x_j}(\rho u_j u_i)=-\dfrac{\partial p}{\partial x_i}+\dfrac{\partial}{\partial x_j}\sigma_{ij}, \\ \dfrac{\partial \rho E}{\partial t}+\dfrac{\partial}{\partial x_j}(\rho u_j E+\rho u_j)=\dfrac{\partial}{\partial x_j}q_j+\dfrac{\partial}{\partial x_j}(u_i\sigma_{ij}). \end{cases} \tag{2.1}$$

Here

$$\sigma_{ij}=\mu_{eff}\left(\frac{\partial u_i}{\partial x_j}+\frac{\partial u_j}{\partial x_i}-\frac{2}{3}\delta_{ij}\frac{\partial u_k}{\partial x_k}\right) \tag{2.2}$$

and

$$q_j=-\lambda_{eff}\frac{\partial T}{\partial x_j} \tag{2.3}$$

are effective stress tensor and effective heat flux vector expressed through partial derivatives of resolved quantities. The effective scalar transport coefficients are represented here simply as:

$$\mu_{eff}=\mu_{lam}+\mu_{sgs}, \tag{2.4a}$$

$$\lambda_{eff}=\lambda_{lam}+\lambda_{sgs}=\frac{\mu_{lam}c_p}{Pr_{lam}}+\frac{\mu_{sgs}c_p}{Pr_{sgs}}, \tag{2.4b}$$

https://doi.org/10.4208/aamm.2014.m829 Published online by Cambridge University Press

where Pr_{sgs} is assumed to be constant and μ_{sgs} is modeled using constant coefficient Smagorinsky SGS model [19]:

$$\mu_T = 2C\rho\Delta^2|\overline{S}|. \tag{2.5}$$

Where $C = C_s^2$, $C_s = 0.1$, Δ-spatial filter width (equal to cell size), $|\overline{S}| = \sqrt{2\overline{S}_{ij}\overline{S}_{ij}}$ and $\overline{S}_{ij} = \frac{1}{2}(\frac{\partial\overline{u}_i}{\partial x_j} + \frac{\partial\overline{u}_j}{\partial x_i})$.

2.2 Numerical scheme

Eq. (2.1) in vector notation reads:

$$\frac{\partial\overline{U}}{\partial t} + \frac{\partial\overline{F}}{\partial x} + \frac{\partial\overline{G}}{\partial y} + \frac{\partial\overline{H}}{\partial z} = 0. \tag{2.6}$$

Spatial derivatives of fluxes in Eq. (2.6) for Cartesian-grid can be expressed by spatial finite differencing operator, as so to retain its conservation property:

$$L_h(\overline{U}^n_{i,j,k}) = \frac{\overline{F}^n_{i-1/2,j,k} - \overline{F}^n_{i+1/2,j,k}}{\Delta x} + \frac{\overline{G}^n_{i,j-1/2,k} - \overline{G}^n_{i,j+1/2,k}}{\Delta y} + \frac{\overline{H}^n_{i,j,k-1/2} - \overline{H}^n_{i,j,k+1/2}}{\Delta z}. \tag{2.7}$$

Inviscid part of fluxes in Eq. (2.7) is evaluated using monotone piecewise-parabolic approximation [20] via diagonalizing of transformation of matrices 5×5 [21]:

$$[A] = [S^{-1}][A][S]. \tag{2.8}$$

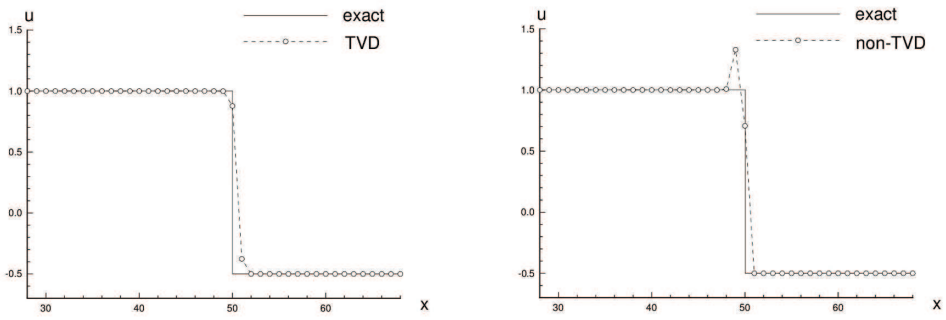
Where $[A]$-Jacobian matrix, $[L]$-diagonal matrix of eigenvalues of $[A]$, and linearized characteristic based approximate Riemann solver [21]. Viscous fluxes are computed from the second order in space central differences.

Computations are advanced in time using two step Range-Kutta scheme,

$$\begin{cases} \overline{U}^{(l)}_{i,j,k} = \overline{U}^n_{i,j,k} + \Delta t L_h(\overline{U}^n_{i,j,k}), \\ \overline{U}^{n+1}_{i,j,k} = \dfrac{1}{2}[\overline{U}^n_{i,j,k} + \overline{U}^{(l)}_{i,j,k} + \Delta t L_h(\overline{U}^{(l)}_{i,j,k})]. \end{cases} \tag{2.9}$$

A minor modification to the source code can convert it to three or higher order method. We give Fig. 1 as a numerical evidence to show that, even with a very nice second order TVD spatial discretization, if the time discretization is by a non-TVD but linearly stable Runge-Kutta method, the result may be oscillatory [22]. Thus it would always be safer to use TVD Runge-Kutta methods for hyperbolic problems. The investigation of TVD time discretization can also be carried out for the generalized Runge-Kutta methods (which have more than one step) [23].

https://doi.org/10.4208/aamm.2014.m829 Published online by Cambridge University Press



(a) TVD time-discretization (b) non-TVD time discretization

Figure 1: Second order TVD MUSCL spatial discretization. Solution after 0.250s.

2.3 Test cases

Using this integration scheme, Chernousov [18] performed two simple test cases: 1) experimentally studied air flow in a turbulent uniform density mixing layer [24] and 2) a turbulent flow in a square duct at $Re = 4800$ [16].

To sustain a turbulent flow regime, velocity field in BC was disturbed randomly in the vicinity of the splitter.

The obtained numerical results, demonstrated a high correlation with the experimental data and the time-independent averaging profiles were quite satisfactory.

2.4 Scheme application

Of particular importance to the development of models for vortex ring dynamics in a real fluid is knowledge of vorticity distribution in the ring. This time-dependent process dictates changes in the volume of fluid, therefore the entrainment is of immediate significance to the unsteady forces that arise due to the presence of vortex rings. Applications ranging from transportation and industry, to animal motion and cardiac flow, are currently being investigated to understand the dynamic role of the observed vortex ring structures. Despite this growing interest, fully empirical measurements of the vortex rings' fluid entrainment have remained elusive. The primary difficulties arise in defining the unsteady boundary of the ring, as well as an inability to maintain the vortex ring in the test section long enough to facilitate measurements. The Cartesian-grid finite volume scheme for compressible unsteady flow can compute shear flow easily and get rid of all experimental difficulties involved.

2.5 Scheme summary

A computational model has been described and applied to LES for the motion and evolution of two isolated vortex rings and their collision in Section 2 The numerical ap-

https://doi.org/10.4208/aamm.2014.m829 Published online by Cambridge University Press

proach based on 3D Cartesian grid Finite Volume Scheme, has been previously verified and applied to vortex dynamics [25]. Firstly, we present the original second order explicit scheme, including a mathematical model Section 2.1, numerical scheme Section 2.2. Further total variation diminishing Runge-Kutta method was explored, where an illustrative numerical example is given to show that it is generally safer to use a TVD Runge-Kutta method for hyperbolic problems [22].

The numerical scheme described in the present section is applied to LES of two isolated vortex rings and their interaction. Hence, two vortex rings head-on collision have been numerically simulated in Section 3, where a detailed discussion of the numerical simulation and results are reported. The effects of variables on motion, deformation and evolution of the vortex rings are investigated. The dynamics of vortex ring and the vorticity distribution are analyzed by means of pressure, velocity field, kinetic energy, entropy, enthalpy, helicity, vorticity iso-surfaces and contour lines, and vortex core properties.

3 Computational results

Being organized in a few sections, this section covers issues in investigations of structure, formation and motion of head-on collision of two vortex rings. The further effects of variables on the evolution, as well as observed phenomenon are also discussed. Due to the no scaling characteristic feature of collision of vortex rings, dimensional variables are used throughout the paper.

3.1 Initial setup

The focus of the present study is to numerically simulate the interaction of two vortex rings interaction and to examine the effect of collision on motion and deformation of two vortex rings. Therefore, the numerical approach just presented in Section 2 was applied to our case.

The initial setup of the colliding simulation consists of two identical coaxial vortex rings placed "upstream" and "downstream" of the plane $x=0$. We focus on the collision of initially perturbed vortex rings. Without perturbation, transition to turbulence was not observed as the rings collided each other, stretching and maintaining perfect axial symmetry. These simulations are thus omitted.

The effects of variables on the evolution of the vortex rings and on the vorticity distribution were investigated by varying, l_x, also as varying V and R of the vortex ring, in the ranges of $6R \leq l_x \leq 12R$, $130 \leq V \leq 260$ and $1.5 \leq r_0 \leq 4$. The best solution will be described in details later on.

Firstly, the centroids of the vortex rings are set at a distance of $l_x = 20D_0$ (ring diameter) away from the plane of collision. This distance was so huge, that during the course of the simulation the vortex rings interact, but no colliding occurred rather sliding. It was found that the best collision cases are achieved when the distance between the rings is from 6 to 12 times their diameter.

https://doi.org/10.4208/aamm.2014.m829 Published online by Cambridge University Press

With $l_x = 17r_0$; the vortex rings are merely convected downstream and upstream by their initial speed without changing its initial orientation. The result agrees with the experimental observation, where the collision was initiated after the two vortex rings had fully formed [1]. This behavior can be explained by velocity, u; and the curl of the velocity u; as we know $u = u_{\inf} + u_2$; where $u_{\inf}$ and u_2 are the velocities of the uni-flow and the vortex ring induction, respectively. It is well known that a circular vortex ring with a uniform vorticity distribution around its core in a fluid at rest at infinity will move along its axis (n) due to its self-induction at the center of the ring, to which all ring elements of unit arc length have the same contribution. When the vortex ring is in a uniform flow $u_{\inf} = 0$, then $u = u_2$; which indicates that the vorticity distribution of the ring does not change. Hence, the ring will move along the vector direction of $u_2 + n$: When the ring is at $l_x > 24r_0$, the ring tilts and deforms as it propagates downstream. However, when $l_x < 24r_0$; the orientation of the ring is reserved. The observed behavior can be explained as follows: a vortex ring traveling in a quiescent fluid is known to entrain surrounding fluid as it propagates downstream [26,27]. The entrainment causes the ring to increase in size with time. When $l_x > 24r_0$, the entrainment of the background vorticity by the vortex core causes vorticity weakening and enhancement on the up-stream and downstream sides, respectively. As a result, the upstream portion of the vortex ring has a lower self-induced velocity when $l_x > 24r_0$ and a higher self-induced velocity when $l_x < 24r_0$. This differential self-induced velocity causes the downstream portion of the vortex ring to tilt and deform before the collision when $l_x > 24r_0$; only sliding occurs. In that study, a vortex rings ejected normal to each other in a rectangular container was observed to tilt and deform more when the rectangular container's length is $l_x > 24r_0$, this behavior is attributed to Coriolis forces and background vorticity; the latter is in line with the present finding. It is worth noting at this point that the interaction between two vortex rings is rather complicated in its details.

Results also showed little change in the shape of the vortex rings during simulation. In particular, the thickness of the ring, appears to remain unchanged. As the rings propagate, the occupied volume expands to include the space between the core and the ring axis. Meanwhile, the ring diameter does not appear to change. After the collision these zones contain little vorticity and appears to have little effect on the dynamics of the vortex cores, so the deformation of the rings remains small. This suggests that within the duration of the simulation the vortex ring remains laminar and the speed was set to 246.667m/s; where we achieved the best results.

3.2 Flow features

Let us consider the evolution of two axisymmetric vortex rings of initial radius r_0. The physical parameters characterizing the vortex rings are summarized in Table 1. The Reynolds number, based on the ring circulation is $Re_\Gamma = \Gamma_0/\nu = 2200$; where n is the kinematic viscosity of fluid; while the Reynolds number based on ring diameter and self-induced translation velocity is $Re_D = 1000$. Prior to the calculations, the ring vorticity

https://doi.org/10.4208/aamm.2014.m829 Published online by Cambridge University Press

Table 1: Flow parameters.

Value	Parameter	Specification	Dimension
50	LEN	Number of cells in length	[-]
140	HIG	Number of cells in height	[-]
140	DEP	Number of cells in depth	[-]
1.0	delta$X$	X-step	[m]
0.8	delta$Y$	Y-step	[m]
0.8	delta$Z$	Z-step	[m]
0.0005	delta$T$	Time step	[sec]
0	Answer	1-continue, 0-start new	[-]
4.500	Computational time	Overall computational time	[sec]
0.0	muL	Dynamic mol. viscosity	[Pa*sec]
0.72	PrL	Molecule Prandtl number	[-]
0.8	PrT	Turbulent Prandtl number	[-]
0.01	C_s	Square of the Smagorinsky C	[-]
717.75	C_v	Heat capacity	[J/(kg*K)]
278.1	R_{gas}	Gas constant	[-]
8.0	V_a	Amplitude of disturbed V	[m/sec]
8.0	W_a	Amplitude of disturbed W	[m/sec]
20	N_{stmin}	Minimal period of disturb	[-]
35	N_{st}	Its max-min	[-]
250	$fstep$	Frame taking step	[-]
70	jc	y-cell coordinate of inlet center	[-]
70	kc	z-cell coordinate of inlet center	[-]
3.0	Radius	Radius of the circular inlet	[m]

is perturbed in the azimuthal direction by displacing the axis of the vortex core using a sine wave perturbation [28]. The bending wave perturbation is specified in terms of its amplitude, W_a, and wave number, N_{st}. As shown in Table 1, a perturbation with $W_a = 8.0$ and $N_{\text{st}} = 12$ is selected [28, 29]. The vorticity distribution of the perturbed vortex ring is initially distributed on a uniform Cartesian mesh of cell size.

Here, we observe the vortex rings motion and quantify the effects of the collision on their structure. The computational domain is a cuboid $l_x \times l_y \times l_z = 50 \times 112 \times 112$; where l_x and l_y are the lateral dimensions of the domain in the horizontal direction and l_z is the dimension in the vertical direction. The two vortex rings of radius r_0 are initially placed "upstream" and "downstream" of the plane $x = 0$. The centroids of the vortex rings are initially at a distance of l_x and 4 ring diameter from the plane of collision. This is analogous to an experiment condition of [1], where two vortex rings were generated experimentally. The velocity conditions have been used at the left and right boundaries, while the periodic condition is imposed at the rest of the boundaries. The computational results are checked for grid sensitivity and it is found that the grid system of $dx \times dy \times dz =$

https://doi.org/10.4208/aamm.2014.m829 Published online by Cambridge University Press

$1.0\times0.8\times0.8$ is sufficient and therefore adopted for all subsequent computations.

3.3 Graphics guide

The general flow features observed in the head-on collision of two coaxial vortex rings are presented as follows. The evolution of the flow is illustrated by plotting at selected time instants the positions of the surfaces of constant values (iso-surfaces). The iso-surfaces are shown in 3D perspective views as 2D scatter plots of projected vortex positions. We generate projections on a stream-wise plane (x-z) and on an azimuthal plane (y-z). The projection planes are used to identify the rate of change of the vortex rings, depicting the projected location and the distance. As can be appreciated from the results below, the stream-wise projections generated in this fashion gives an illustration of secondary motion, while (y-z) projections effectively depict an azimuthal slice of the vortex core.

The simulation was conducted to demonstrate the vortex rings collision within the volume for longer periods of time, with the goal of observing ring growth due to fluid entrainment. The evolution of the vortex rings is illustrated in figures, which shows the distribution of the iso-surfaces at selected times, and depicts three-dimensional perspective views of these iso-surfaces. The iso-surfaces are plotted using different flood and contour lines. These data enabled definition of the unsteady boundary of the vortex rings for transient entrainment calculations.

The obtained results are plotted in figures at selected time instants. We collect the data information at 12 physical times, i.e., 0.125s, 0.500s, 0.750s, 1.000s, 1.250s, 1.500s, 1.750s, 2.000s, 2.250s, 2.500s, 2.750s and 3.000s, respectively. In the following discussion, physical times are used as the x-axis. Being organized in few frames, the figures cover issues in describing the structure, formation and motion of the collision, using the distribution of the following parameters: density, pressure, velocity, kinetic energy, entropy, enthalpy, helicity, vorticity.

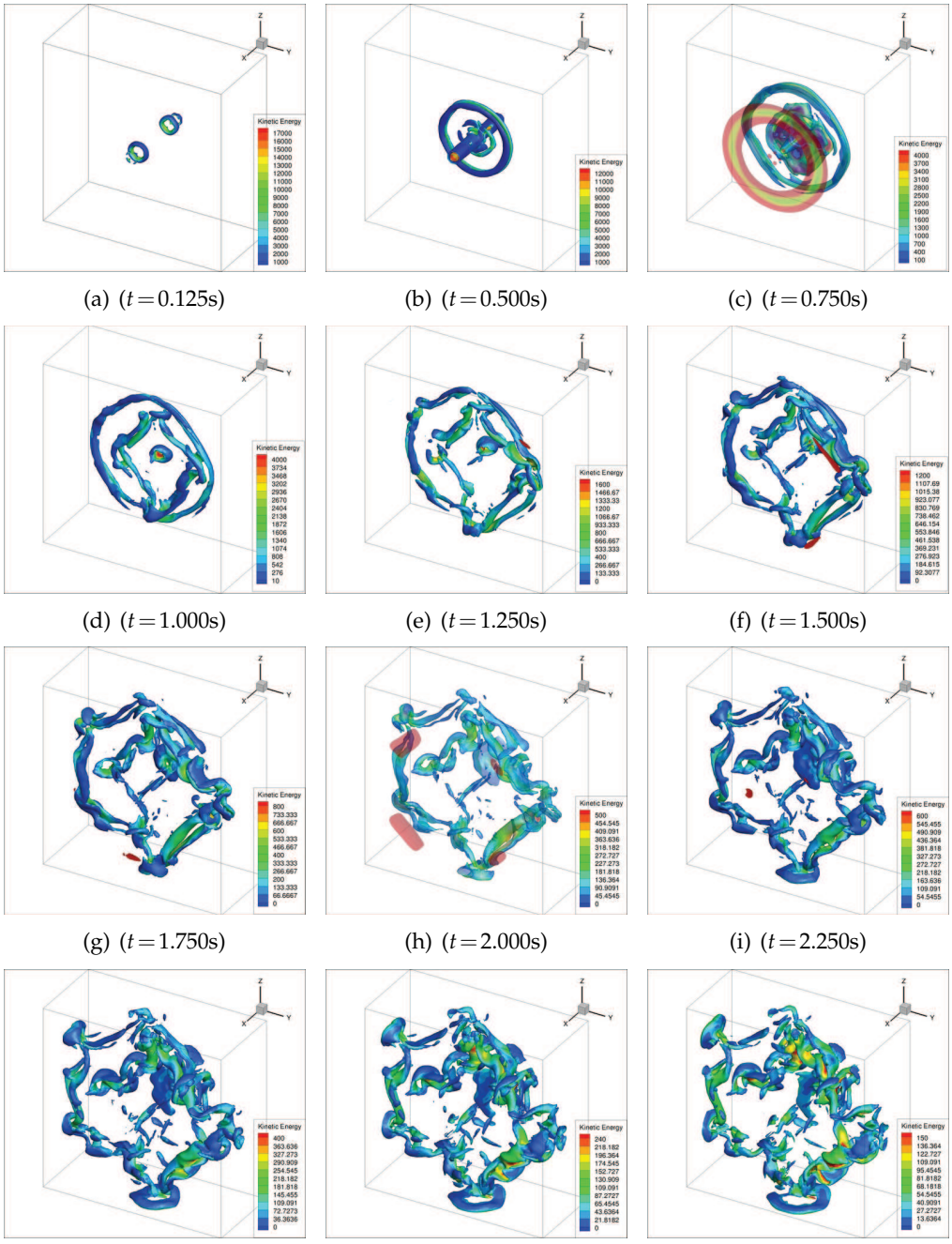
3.4 Physics

We present three dimensional Cartesian view of vorticity iso-surfaces, filled with kinetic energy flood, shown in Fig. 2. Fig. 9(h) is presenting the magnitude at the selected iso-surfaces $\text{vorticity}_{\text{iso}}$ as well as the minimum, the maximum and the whole volume average values, as a function of time.

In the early stages of the simulation the rings are well separated and the interaction is weak. Thus, in discussing the results we omit the early stages of approach towards the plane of collision and focus exclusively on the later stages.

In the early stages of the simulation Fig. 2(a), the rings propagate under their own self-induced motion, and the low vorticity are left in the wakes of the rings. As the rings approach each other, their translation velocity decreases while their radii increase. As discussed later, this also leads to significant increase in the entrophy. By 1.000s, Fig. 2(d) the two rings can no longer be distinguished as they have completely merged into a

https://doi.org/10.4208/aamm.2014.m829 Published online by Cambridge University Press



(a) ($t=0.125$s) (b) ($t=0.500$s) (c) ($t=0.750$s)

(d) ($t=1.000$s) (e) ($t=1.250$s) (f) ($t=1.500$s)

(g) ($t=1.750$s) (h) ($t=2.000$s) (i) ($t=2.250$s)

(j) ($t=2.500$s) (k) ($t=2.750$s) (l) ($t=3.000$s)

Figure 2: Kinetic energy flood in vorticity iso-surfaces, in 3D Cartesian view, at 0.125s–3.000s.

https://doi.org/10.4208/aamm.2014.m829 Published online by Cambridge University Press

single doughnut-shaped structure. This structure continues to extend in radial direction, leaving a web of clouds around the centers. Like the clouds left in the wakes of the approaching rings, these clouds carry little vorticity and have consequently little effect on the dynamics of the concentrated cores. Fig. 2 shows that at different time the clouds have clumped into different groups spaced azimuthally. The center clumping is not evident in the last 3.000s, presented by Fig. 2(l) which also shows that the center clouds are not stable and appear to be a temporary clumps.

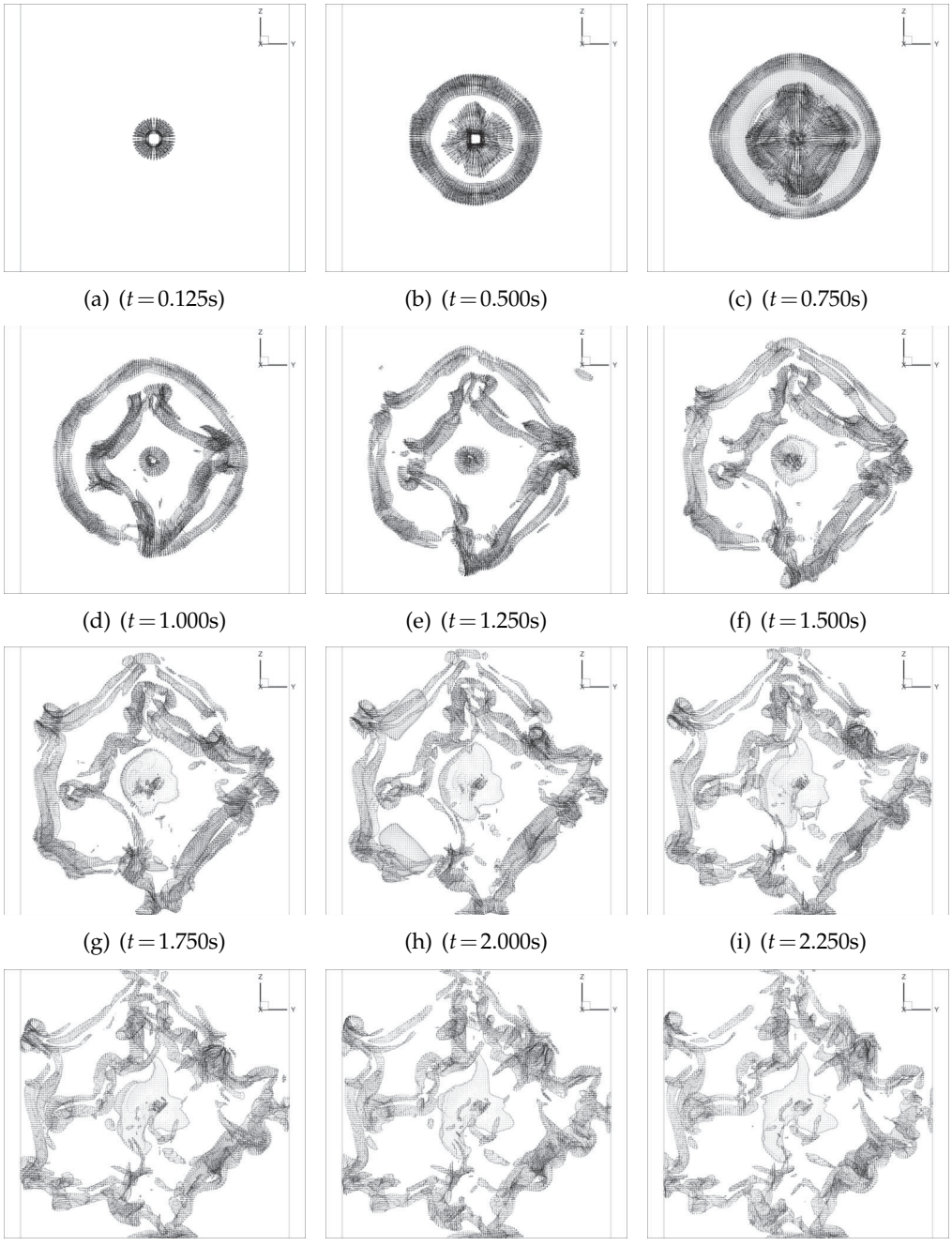
Fig. 3 shows velocity field distribution of the same vorticity iso-surfaces as Fig. 2 at the selected times in (y-z) plane. One can clearly see that the distribution of velocity during the simulation is changing in a big range, which can be easily appreciated by observing Fig. 9(c), where the velocity values are presented as a function of time. In the early stages of the collision 0.500s-0.750s, shown in Figs. 3(b), 3(c) the velocity is concentrated in the initial cores of the rings. As their radii increase, the velocity field disperses in a radial direction and decrease in magnitude. In the interval 1.000s-1.500s, the doughnut-shaped structure continues to extend in radial direction Figs. 3(d)-3(f), leaving a web of clouds around the centers. Little by little, in the 1.750s-2.250s, the velocity field in these clouds disperses away from the center far in radial direction, where the rings start to break down and concentrate in the periphery Figs. 3(g)-3(i). In the late stages Figs. 3(k)-3(l), corresponding to 2.500s-3.000s, the velocity distribution already is mainly concentrated in the places, where obviously new structure start to form. This shows that the velocity distribution during the simulation is directly connected with the vorticity distribution observed in Fig. 2 and change accordingly. Furthermore, one can observe the little clouds in the center, the stretching of the vortex rings, their merger and the generation of distinct new clusters.

Fig. 4 shows vorticity flood in enthalpy iso-surfaces at the selected times in (y-z) plane. The distribution of the vorticity during the simulation is qualitatively similar to that observed in Fig. 2 and Fig. 3, but here it can be inspected more detailed. Close examination of the results suggests that, as observed above, in the early stages of the collision 0.125s-1.250s stretching of the two initial rings during collision does occur, but at a slower rate Figs. 4(a)-4(e); and opposite, at a faster rate in 1.500s-1.750s when the breakdown occurs Figs. 4(f), 4(g). One can also observe that the clumps in the center disperse much faster than in Figs. 3(g)-3(i).The new clumps of eddies start to merge at 1.500s at the outer part Fig. 4(f), and appears to form quickly to 2.250s, Fig. 4(i) into organized ringlet structures and after that in the final stages of the collision just grow in diameter.

These observation are confirmed from the next Fig. 5, where vorticity flood in the same enthalpy iso-surfaces is presented in (x-z) plane. In particular, the initial stages of the motion, the deceleration and the increase in ring diameter, and the subsequent merger of the rings are clearly depicted. In addition, the surface plots also enable us to further characterize the late stages of the collision. In particular, the results show that the clumping of particles observed earlier is in fact associated with vortex reconnection, which leads to the formation of small-scale structures. Let us distinguish these phenomena.

At 1.000s the colliding rings can still be distinguished, see Fig. 4(d) and Fig. 5(d),

https://doi.org/10.4208/aamm.2014.m829 Published online by Cambridge University Press



(a) ($t=0.125$s) (b) ($t=0.500$s) (c) ($t=0.750$s)

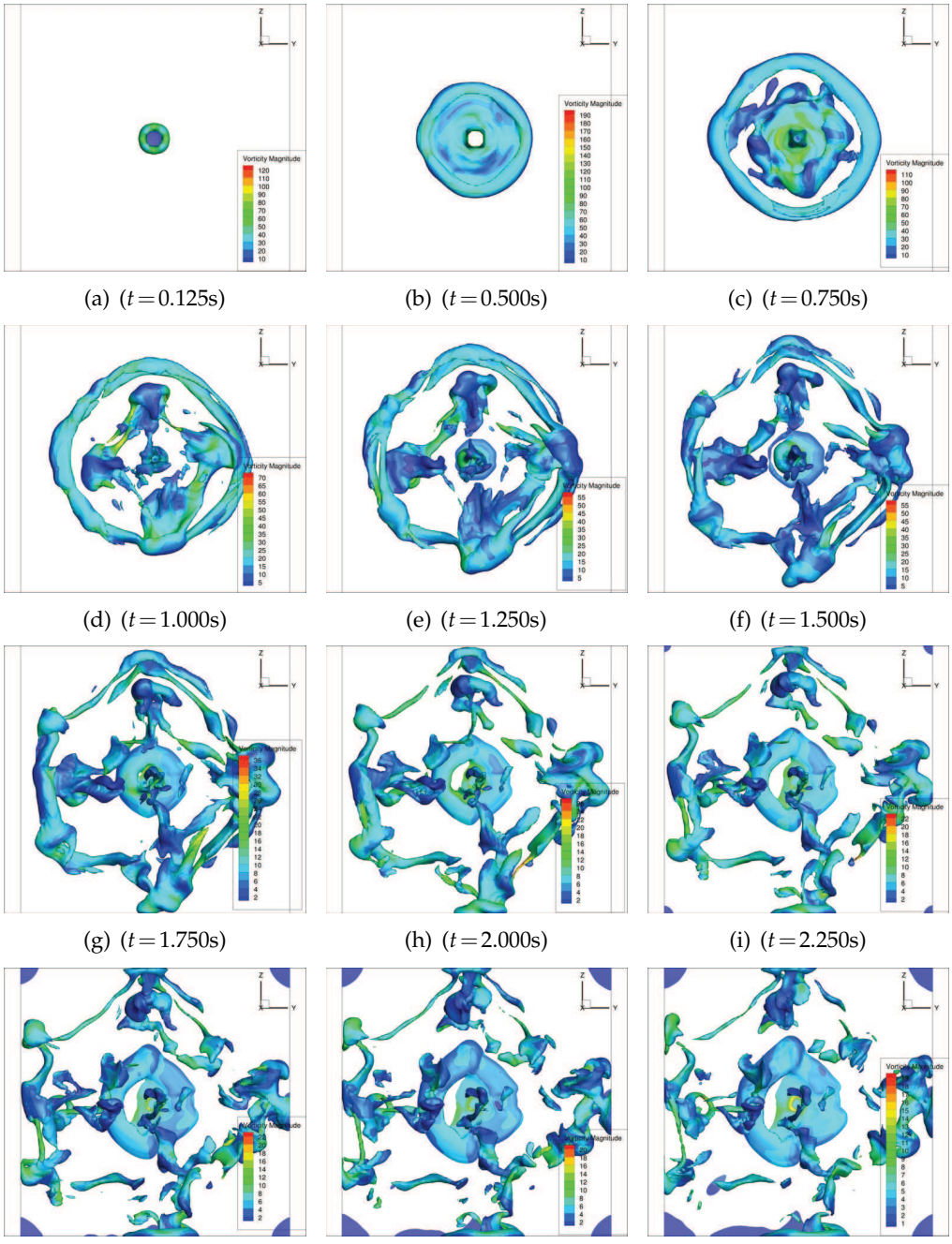
(d) ($t=1.000$s) (e) ($t=1.250$s) (f) ($t=1.500$s)

(g) ($t=1.750$s) (h) ($t=2.000$s) (i) ($t=2.250$s)

(j) ($t=2.500$s) (k) ($t=2.750$s) (l) ($t=3.000$s)

Figure 3: Velocity field in vorticity iso-surfaces, in (y-z)-plane, at 0.125s–3.000s.

https://doi.org/10.4208/aamm.2014.m829 Published online by Cambridge University Press



(a) ($t=0.125$s) (b) ($t=0.500$s) (c) ($t=0.750$s)

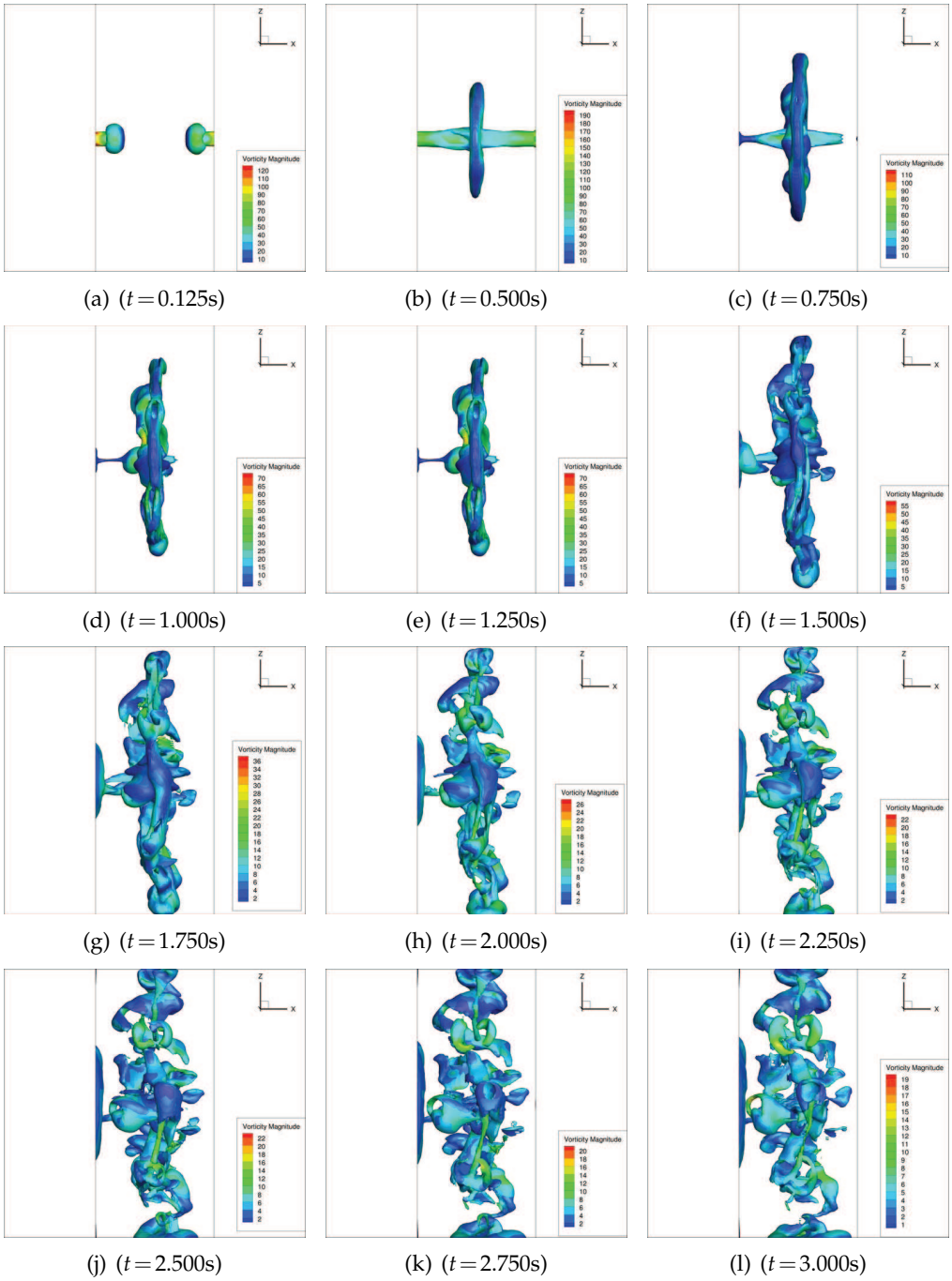
(d) ($t=1.000$s) (e) ($t=1.250$s) (f) ($t=1.500$s)

(g) ($t=1.750$s) (h) ($t=2.000$s) (i) ($t=2.250$s)

(j) ($t=2.500$s) (k) ($t=2.750$s) (l) ($t=3.000$s)

Figure 4: Vorticity flood in enthalpy iso-surfaces, in (y-z)-plane, at 0.125s–3.000s.

https://doi.org/10.4208/aamm.2014.m829 Published online by Cambridge University Press



(a) ($t=0.125$s) (b) ($t=0.500$s) (c) ($t=0.750$s)

(d) ($t=1.000$s) (e) ($t=1.250$s) (f) ($t=1.500$s)

(g) ($t=1.750$s) (h) ($t=2.000$s) (i) ($t=2.250$s)

(j) ($t=2.500$s) (k) ($t=2.750$s) (l) ($t=3.000$s)

Figure 5: Vorticity flood in enthalpy iso-surfaces, in (x-z)-plane, at 0.125s–3.000s.

https://doi.org/10.4208/aamm.2014.m829 Published online by Cambridge University Press

although separation already started and early signs of reconnection can be detected. By 2.250s however, see Fig. 4(i) and Fig. 5(i), distinct reconnected vortical structures have formed, and the original rings no longer exist. Specifically, in Fig. 4(f) and Fig. 5(f), new reconnection can be observed clearly at 1.500s. By the end of the simulation, 2.000s-3.000s the (x-z) view Figs. 4(g), 4(l) and Figs. 5(g), 5(l), shows the presence of distinct vortical structures, which correspond to the clumps seen early in Fig. 2 and Fig. 3.

As shown in Fig. 2 and Fig. 3. the details of the reconnection are significantly analogues and corresponding to the distribution shown in Fig. 4. At 2.500s the original rings have totally disappeared, leaving a disorderly collection of smaller-scale vortical structures. On the other hand, the growth of the new formed structures occurs at 2.000s-3.000s. Significant appears to take place before the final stages, where only weak and disorganized structures remain.

In all cases considered the head-on collision of the vortex rings naturally leads to the generation of small-scale flow structures and consequently strains the resolution of the computations.

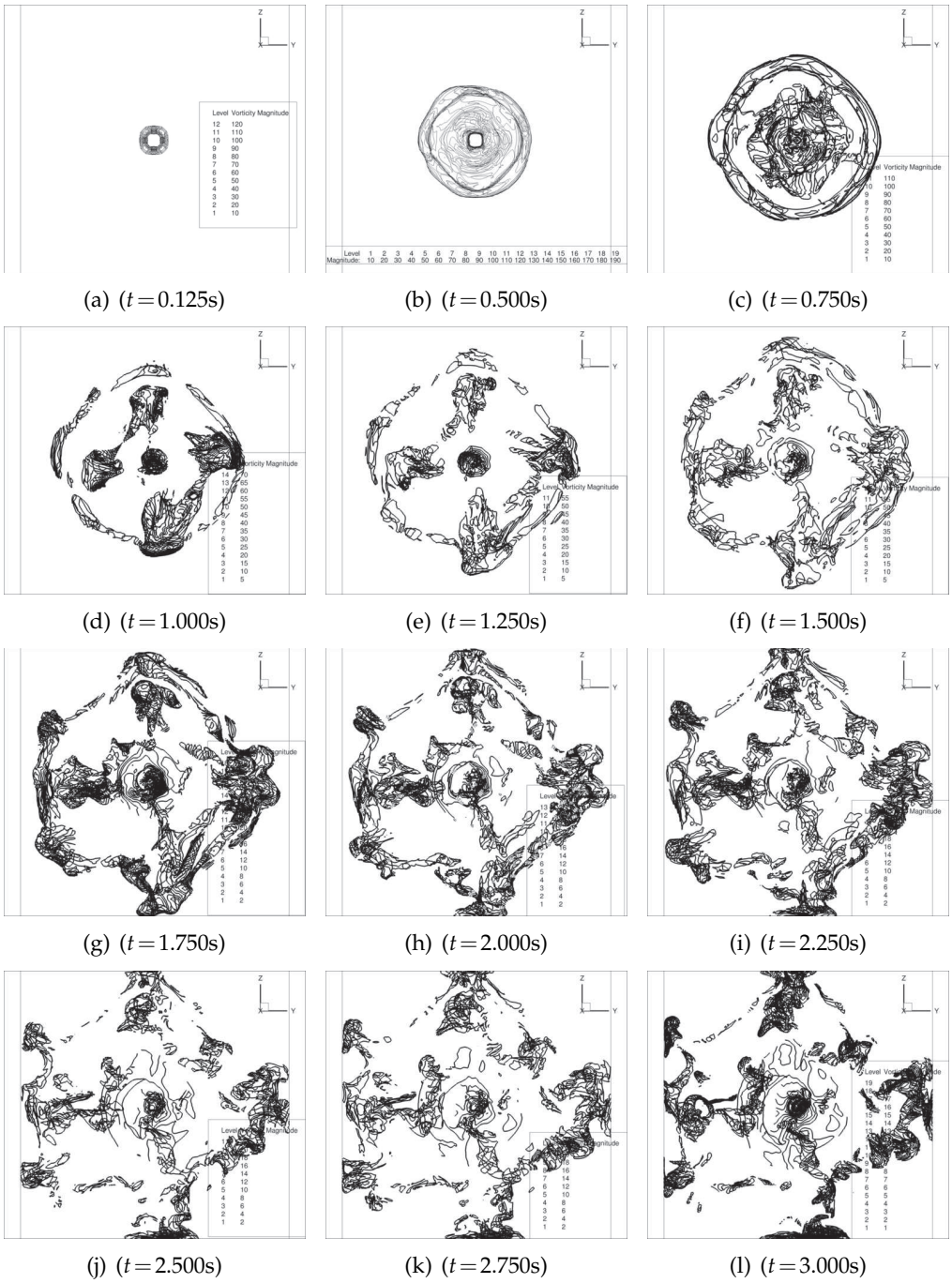
3.5 Rotation and deformation

The vorticity distribution of the new formed ringlets clearly shows organization in a manner suggestive of turbulence. Additional insight into the evolution of the new formed ringlets is gained by generating the density iso-surfaces, filled with vorticity contour lines. This provides us with another illustration of the various stages of the head-on collision of the vortex rings. The vorticity contours for the different time are shown in Fig. 6 in (y-z) plane.

It is found that in the early stages, the vorticity contour lines around the ring spreads around it asymmetric way, see Figs. 6(b)-6(d), but as time increases, they spreads around it non symmetrically. Obviously, there is a difference in the cross-sectional size of the new formed ringlets on the 12 and 6 o'clock sections, as well as the one in the 3 and 9 o'clock. Thus, a vorticity gradient is generated along the ringlets, resulting in a deformation and elongation, in the radial direction, of the original vortex rings. It can be seen that the collision causes breakdown in symmetry, leading to the deformation and tilting of the vortex rings. Our computation further shows that an increase in the radial direction of the new ringlets results in increasing of the tilting angle. This was also observed experimentally by Lim [1].

For completeness, we also compute the helicity iso-surfaces filled with vorticity flood, shown in Fig. 7. One can clearly see that the distribution of helicity during the simulation is changing in a big range, while the vorticity magnitude almost does not change. In the early stages of the collision 0.5s-0.75s, shown in Figs. 7(b), 7(c) the helicity is concentrated in the initial cores of the rings, leaving a web of clouds around the centers. As their radii increase, the helicity translate in a radial direction. In the interval 1.000s-1.500s the helicity cloud structure continues to extend in radial direction Figs. 7(d)-7(f). By 1.750s-2.250s the velocity field in these clouds disperse away from the center far in radial direction,

https://doi.org/10.4208/aamm.2014.m829 Published online by Cambridge University Press



(a) ($t=0.125$s) (b) ($t=0.500$s) (c) ($t=0.750$s)

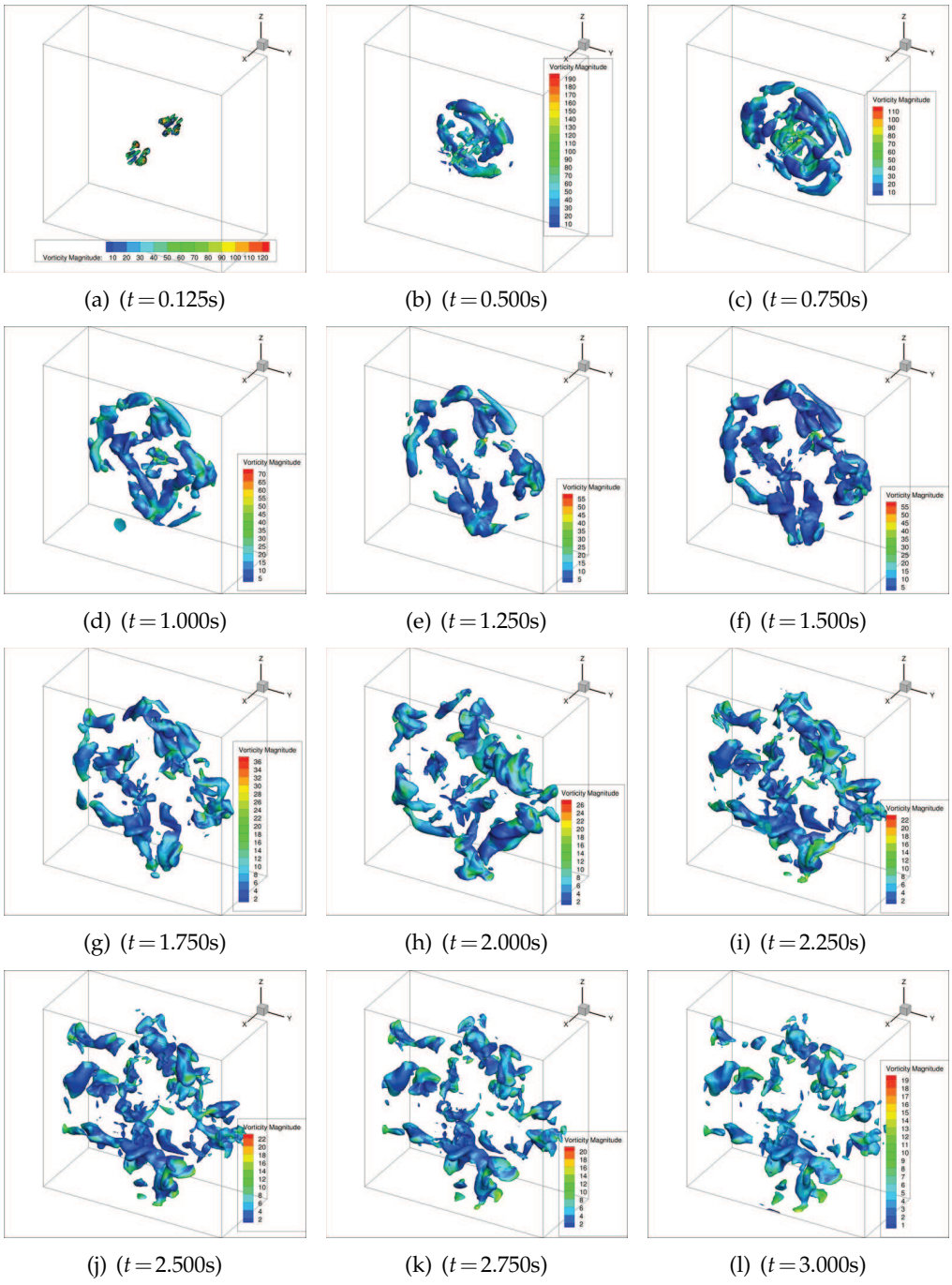
(d) ($t=1.000$s) (e) ($t=1.250$s) (f) ($t=1.500$s)

(g) ($t=1.750$s) (h) ($t=2.000$s) (i) ($t=2.250$s)

(j) ($t=2.500$s) (k) ($t=2.750$s) (l) ($t=3.000$s)

Figure 6: Vorticity lines in density iso-surfaces, in (y-z)-plane, at 0.125s–3.000s.

https://doi.org/10.4208/aamm.2014.m829 Published online by Cambridge University Press



(a) ($t=0.125$s) (b) ($t=0.500$s) (c) ($t=0.750$s)

(d) ($t=1.000$s) (e) ($t=1.250$s) (f) ($t=1.500$s)

(g) ($t=1.750$s) (h) ($t=2.000$s) (i) ($t=2.250$s)

(j) ($t=2.500$s) (k) ($t=2.750$s) (l) ($t=3.000$s)

Figure 7: Vorticity flood in helicity iso-surfaces, in 3D Cartesian view, at 0.125s–3.000s.

https://doi.org/10.4208/aamm.2014.m829 Published online by Cambridge University Press

where the rings start to concentrate in the at the edges of the breakdown of the original rings Figs. 7(g)-7(i).

It can be seen that the collision causes breakdown in symmetry from the early beginning, leading to the deformation and tilting of the helicity. Our computation further shows that an increase in the radial direction of the new ringlets results in the helicity tilting. In the late stages Figs. 7(k)-7(l), corresponding to 2.500s-3.000s, the helicity distribution already is mainly concentrated in the places, where we already saw that new structure are form. This shows that the helicity distribution during the simulation is directly connected with the vorticity concentration and change accordingly. Furthermore, the stretching of the vortex rings, their merger and the generation of distinct new ringlets can be observed easy by the helicity distribution, which can be used to locate the region where new structures will be formed. This can be most easily appreciated by comparing Fig. 2 and Fig. 7 at corresponding time instants.

We finally note that in all cases considered the head-on collision of the vortex rings naturally leads to the generation of small-scale flow structures. This phenomenon is affected by a variety of phenomena, including the radial stretching of the large-eddy cores, amplification of 3D instabilities, vortex merger and reconnection. The effect of small-scale structures on the behavior of the solution, and the role of the turbulence model are further discussed below.

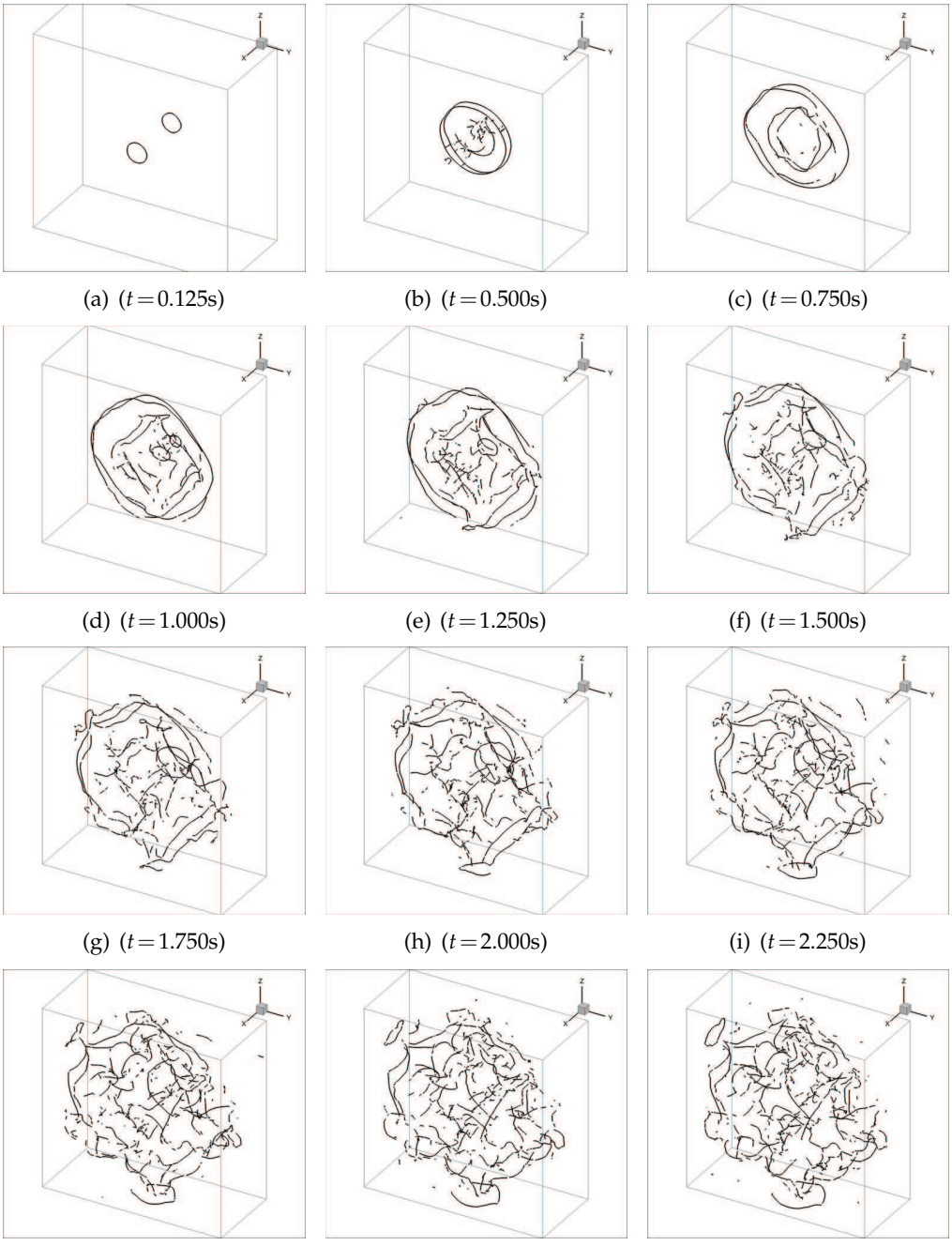
3.6 Evolution

To gain further insight into the vortex evolution, we present different solutions Fig. 9, which give us information about the evolution of the vortex ring in time. The minimum, the maximum, the whole volume average and the vorticity iso-surface average values of the parameters: density, pressure, velocity, kinetic energy, entropy, enthalpy, helicity, vorticity, vortex cores position and diameter are presented as a function of time. The recorded average values are calculated directly according to Tecplot database. The blue square line presents the minimum value $X_{\min}$, the red rhombus line–the maximum $X_{\max}$, the pink line X_{aver}–the average in the whole volume, the black triangle line X_{iso}–the average in the vorticity iso-surface.

In all cases considered, see Figs. 9(a)-9(h), the blue square line presenting the minimum value and the pink noble line presenting the average in the whole volume values of the most parameters are pretty near. Here, the subscript min, max, and aver represent the minimum, maximum and average values of the variables, respectively. Namely $P_{\min}$ and P_{aver}; $V_{\min}$ and V_{aver}; $E_{k\min}$ and $E_{k\text{aver}}$; $\text{Enthalpy}_{\min}$ and $\text{Enthalpy}_{\text{aver}}$; $\text{Vorticity}_{\min}$ and $\text{Vorticity}_{\text{aver}}$; they have even the same progress in time. Just a little difference exists only between $\text{Entropy}_{\min}$ and $\text{Entropy}_{\text{aver}}$, but considering the other values this also can be counted as pretty near. So we can conclude that the pressure, velocity, kinetic energy, entropy, enthalpy and vorticity values, all are concentrated in the vorticity iso-surface, as expected.

Big difference can be extinguished between $r_{\min}$ and r_{aver}, where the average value

https://doi.org/10.4208/aamm.2014.m829 Published online by Cambridge University Press



(a) ($t=0.125$s) (b) ($t=0.500$s) (c) ($t=0.750$s)

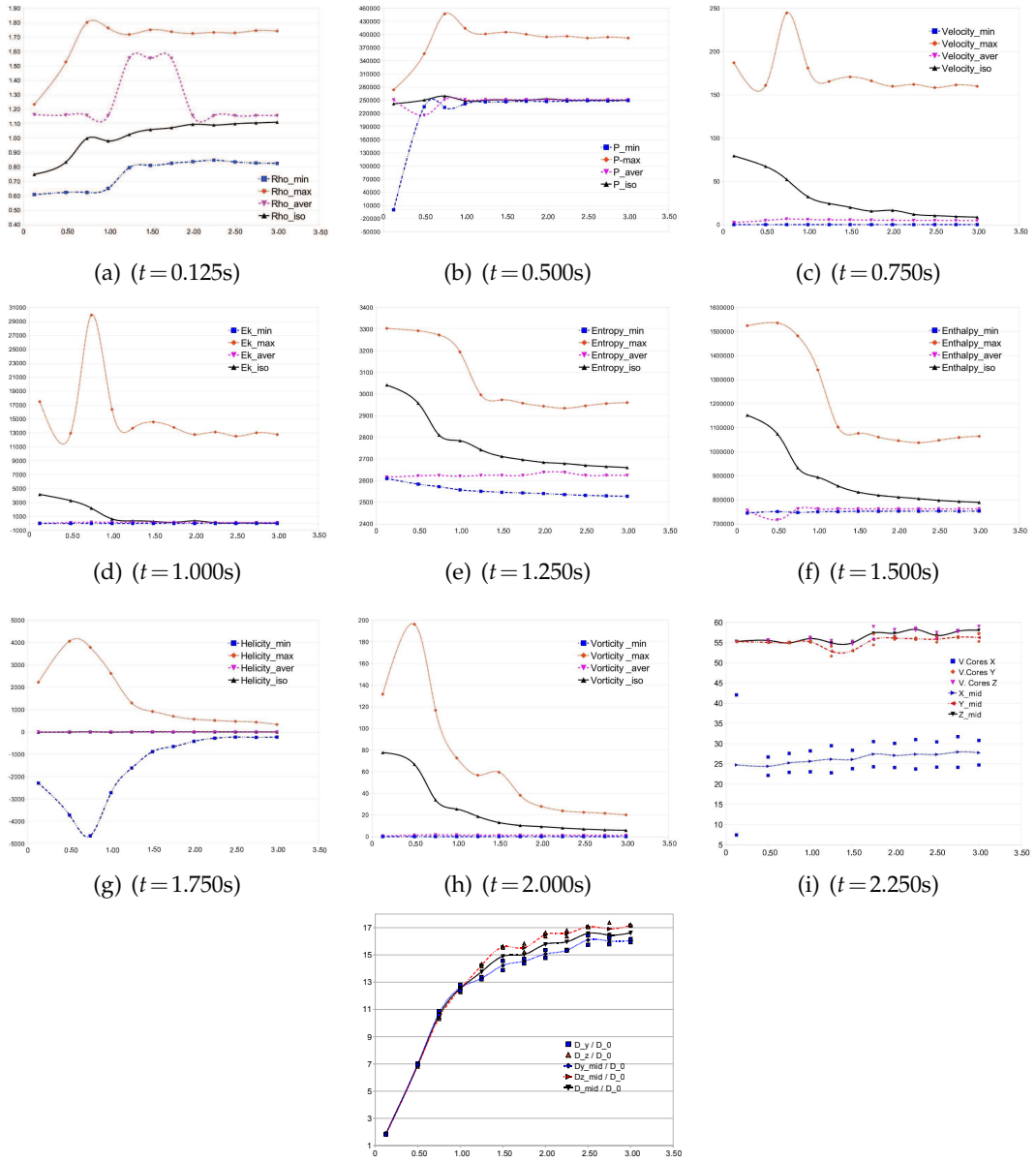
(d) ($t=1.000$s) (e) ($t=1.250$s) (f) ($t=1.500$s)

(g) ($t=1.750$s) (h) ($t=2.000$s) (i) ($t=2.250$s)

(j) ($t=2.500$s) (k) ($t=2.750$s) (l) ($t=3.000$s)

Figure 8: Vortex core in 3D Cartesian view, at 0.125s–3.000s.

https://doi.org/10.4208/aamm.2014.m829 Published online by Cambridge University Press



(a) ($t=0.125$s) (b) ($t=0.500$s) (c) ($t=0.750$s)

(d) ($t=1.000$s) (e) ($t=1.250$s) (f) ($t=1.500$s)

(g) ($t=1.750$s) (h) ($t=2.000$s) (i) ($t=2.250$s)

(j) ($t=2.500$s)

Figure 9: The minimum, maximum and average values, at 0.125s–2.500s.

is located in the middle between $r_{\min}$ and $r_{\max}$ with a huge jump from with a plateau 1.000s-2.000s, which is more near to $r_{\max}$. Then the plateau drops back to its initial values, see Fig. 9(a). The value $r_{\min}$ gradually increases with one little jump form 1.000s-1.250s. The value rises gradually increases accordingly, but the little jump is earlier at 0.500s-

https://doi.org/10.4208/aamm.2014.m829 Published online by Cambridge University Press

0.750s, and is followed by slowly decrease 0.750s-1.000s, after that $r_{\min}$ proceed with its gradually increase. In the other hand $r_{\max}$ starts with fast rise to 0.750s, then decreases slowly to 0.750s, and after that is stable with just small fluctuations.

The situation with helicity is complicated by the fact that the values have positive and negative values, see Fig. 9(g). $\text{Helicity}_{\text{iso}}$ and $\text{Helicity}_{\text{aver}}$ have been merge in one line, as the $\text{Helicity}_{\min}$ and $\text{Helicity}_{\max}$ values are symmetric with reference line 0 and have almost the same progress in time, starting with a fast rise (the module value), and reach a peak about 0.750s, soon thereafter, decreases with the same speed up to 1.250s, then decreases gradually for the rest of the simulation.

In the early stages of simulation the plots of $P_{\min}$ have a fast jump up to the maximum values at 0.500s, than a small drop to 1.000s, followed by more stable stage, see Fig. 9(b). The $P_{\max}$ has almost the same pattern with the slight difference in the initial speed of increasing, which is little bit slower than the one in $P_{\min}$. So the maximum peak is reached at 0.750s, followed by fast decrease to 1.000s. The big difference between $P_{\min}$ and $P_{\max}$ is the initial value, which is much bigger for $P_{\max}$. The average pressure in the whole volume P_{aver}, has one little drop at 0.500s. The average pressure in the vorticity iso-surface P_{iso} is almost stable, except one tinny jump near 0.750s.

One can perceive clearly from Figs. 9(c), 9(d) that the velocity and the kinetic energy profiles has almost the same progress in time. In the early stages of simulation both $V_{\max}$ and $E_{k\max}$ start with fast drop up to 0.500s, where they reach a minimum value, than two time faster jump to the maximum value at 0.750s, than fast drop again to 1.250s and gradually decreases for the rest of the simulation. The average velocity in the vorticity iso-surface V_{iso}, and the average kinetic energy in the vorticity iso-surface $E_{k\text{iso}}$ both starts with its maximum and decreases slowly to 1.000s, after which gradually decreases with tinny fluctuations for the rest of the simulation. In the late stages, after 2.250s, both tend to the minimum and average values of the whole volume. Both V_{iso} and $E_{k\text{iso}}$ concentrated in the vorticity iso-surface has its maximum at the beginning where the jet has its powerful blow and decreases, matching the inertial forces recession.

Entropy:

$$s = C_v \ln\left(\frac{p}{p_\infty}\right) + C_p \ln\left(\frac{p_\infty}{p}\right). \tag{3.1}$$

Where, Specific heat at constant pressure: $C_p = \frac{\gamma R}{\gamma - 1}$ and Ratio of specific heats: $\gamma = \frac{C_p}{C_v}$,

Enthalpy per unit mass:

$$h = C_p T. \tag{3.2}$$

X-, Y-, Z- Vorticity:

$$\begin{bmatrix} \omega_x \\ \omega_y \\ \omega_z \end{bmatrix} = \begin{bmatrix} \dfrac{\partial w}{\partial y} - \dfrac{\partial v}{\partial z} \\ \dfrac{\partial u}{\partial z} - \dfrac{\partial w}{\partial x} \\ \dfrac{\partial v}{\partial x} - \dfrac{\partial u}{\partial y} \end{bmatrix}. \tag{3.3}$$

https://doi.org/10.4208/aamm.2014.m829 Published online by Cambridge University Press

Vorticity Magnitude:

$$\|\boldsymbol{\omega}\| = \sqrt{\omega_x^2+\omega_y^2+\omega_z^2}. \tag{3.4}$$

One can also discern from Figs. 9(e), 9(f) that the entropy and enthalpy profiles have very similar progress in time. In the early stages of simulation both $\text{Entropy}_{\max}$ and $\text{Enthalpy}_{\max}$ start with plateau and fast drop from 0.750s to 1.250s, than gradually decreases to 2.250s, where has their minimum value, and than increases very slowly for the rest of the simulation. The average values in the vorticity iso-surface $\text{Entropy}_{\text{iso}}$ and $\text{Enthalpy}_{\text{iso}}$, also follow one pattern. Both starts with their maximum and decreases fast to 0.750s, after which decreases slower to 1.500s, and gradually decreases for the rest of the simulation.

The indication from the vorticity record Fig. 9(h) shows that in the early stages of simulation $\text{Vorticity}_{\max}$ start with fast jump up to 0.500s, where reach a maximum value, than faster drop to 1.250s, than little jump again to 1.500s, followed by faster drop to 2.000s and gradually decreases for the rest of the simulation. The average value in the vorticity iso-surface $\text{Vorticity}_{\max}$, follow the pattern of $\text{Entropy}_{\text{iso}}$ and $\text{Enthalpy}_{\text{iso}}$. It starts with its maximum and decreases fast to 0.750s, after which decreases slower to 1.500s, and gradually decreases for the rest of the simulation. $\text{Vorticity}_{\text{iso}}$ has its maximum at the beginning where the jet has its powerful blow and decreases slowly, matching the inertial forces recession.

The results indicate that the entrainment process consists of a rapid convection-based entrainment phase during new ring formation, followed by a slower diffusive mechanism that entrains ambient fluid into the vortex rings. The evolutions of the growth rate of vortex ring and vorticity distribution are used to explain those observed effects.

Furthermore, we will observe the vortex cores position and diameter Figs. 9(i), 9(j) as a function of time, which give us information evolution of the vortex cores.

Fig. 9(i) shows the vortex cores center position and their average value, as a function of time. The blue squares V. Core X presents the exact vortex cores center in X direction, while X_{mid} is their average value, presented as a blue triangle line. The red rhombus V. Core Y presents the exact vortex cores center in Y direction, while Y_{mid} their average value is presented as red trianlge line. The pink V. Core Z presents the exact vortex cores center in Z direction, while Z_{mid} their average value is presented as black line.

Fig. 9(j) shows the vortex cores diameters and their average value, as a function of time. The blue squares Dy presents the exact vortex cores diameters in Y direction, while Dy_{mid} their average value is presented as a blue line. The red rhombus Dz presents the exact vortex cores diameters in Z direction, while Dz_{mid} their average value is presented as red triangle line. The black line D_{mid} presents the average value between the diameters Dy_{mid} and Dz_{mid}.

3.6.1 Turbulence eddy viscosity

For the purpose of quantifying the effect of the dynamic model on the simulation, we examine the spatially averaged turbulence eddy viscosity μ_T. Recall that μ_T formulate

https://doi.org/10.4208/aamm.2014.m829 Published online by Cambridge University Press

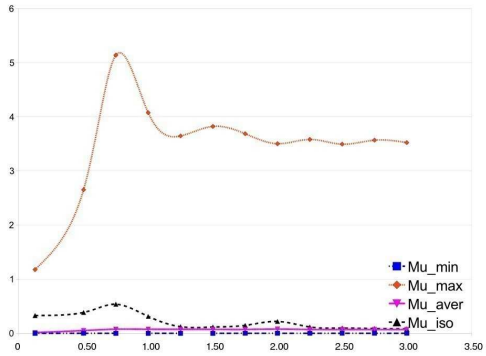


Figure 10: The minimum, maximum, average values of μ_T, in the vorticity iso-surface and whole volume, as a function of time.

is indicated in Eq. (2.5). Fig. 10 shows instantaneous values of the turbulence eddy viscosity, plotted are curves for the minimum $\mu_{\min}$, maximum $\mu_{\max}$, average values in the whole volume μ_{aver} and vorticity iso-surface μ_{iso}, as a function of time. As mentioned above, the calculations were performed both in the whole volume and in isolated vorticity iso-surface. The average turbulence eddy viscosity values are calculated according to Eq. (3.5).

$$\mu_T = \frac{\sum_i [\mu_T(X_i)] dV_i}{\sum_i dV_i}. \tag{3.5}$$

Fig. 10 shows that $\mu_{\max}$ is close to 1 at the start of the calculation. In the early stages, the computed estimate of $\mu_{\max}$ first increase fast, reaching a peak around 5 at 0.750s and then drops to 4 at 1.000s. Soon thereafter, the curves for $\mu_{\max}$ increase to 3.8 at 1.500s and then drops back to 3.5 at 2.000s. At later times, the behavior of the curve $\mu_{\max}$ remains close to 3.5, with little fluctuations. The turbulent eddy viscosity indicates that the vortex rings are not turbulent. The colliding only experience a degree of turbulence during their collision, which then dies off and it appears to last for a short time.

The evolution of maximum turbulence eddy viscosity in the whole volume can be most easily appreciated by observing Fig. 11 at corresponding vorticity values. Apparently, $\mu_{\max}$ increases, from 3.5 to 5.3, with the increase of the maximum vorticity from 20 to 120, reaching its maximum value. Then $\mu_{\max}$ decrease fast to 1, and reaches its minimum, where the $\text{Vorticity}_{\max}$ is 135. At later stage $\mu_{\max}$ increases slowly up to 2.6, where $\text{Vorticity}_{\max}$ has its maximum value 200.

In the vorticity iso-surface, see Fig. 12, μ_{iso} increases from 0.07 to 0.23, about three times ofits initial value, with the increase of the average vorticity in the iso-surface from 5 to 10; reaching a little peak. Then μ_{iso} decreases almost to its initial value, where the $\text{Vorticity}_{\text{iso}}$ is 15. Furthermore, μ_{iso} increases, reaching its maximum value 0.54, with the increase of the vorticity from 15 to 35. Than $\mu_{\max}$ steadily decrease to 0.33, where the $\text{Vorticity}_{\max}$ has his maximum value 77.

Comparing Fig. 11 and Fig. 12, one can see that the maximum value of turbulence

https://doi.org/10.4208/aamm.2014.m829 Published online by Cambridge University Press

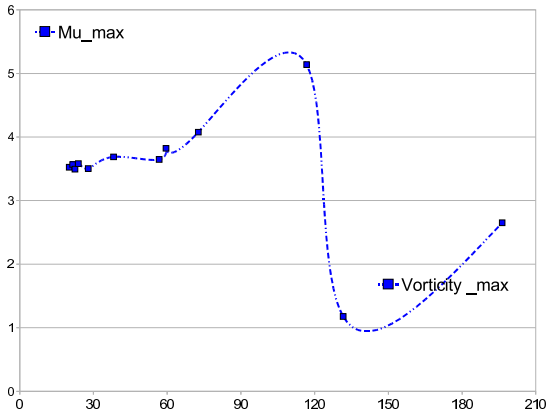


Figure 11: $\mu_{\max}$ is a function of the maximum vorticity.

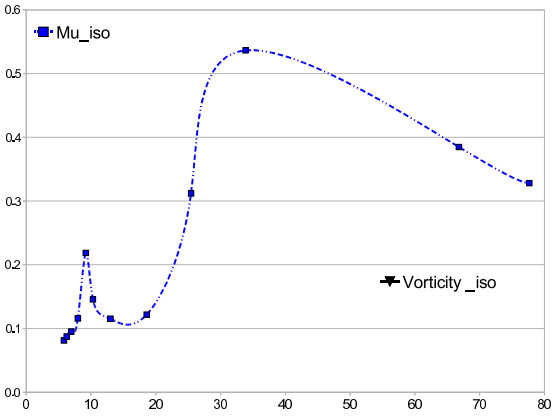


Figure 12: μ_{iso} is a function of the average vorticity in the iso-surface.

eddy viscosity for the whole volume, $\mu_{\max}$ is about 10 times higher than the maximum in the vorticity iso-surface μ_{iso}. The minimum value of $\mu_{\max}$ is also 10 times higher than μ_{iso}. Apparently, both $\mu_{\max}$ and μ_{iso} show a plateau, which is located in some middle value of the vorticity magnitude.

The variation of the eddy viscosity is dominated by changes in the vorticity, whose relative variation has much greater range in the whole volume than that in the vorticity iso-surface. The turbulence eddy viscosity controls the spatial locations where the influence of the turbulence model is being experienced, as seen in the breakdown of the volume into quintiles according to vorticity magnitude. In low vorticity regions the turbulent eddy viscosity can be one or two orders of magnitude smaller than in high vorticity regions.

The evolution of the vortex cores can be most easily appreciated by observing the rings radii stretching Fig. 8 at corresponding time instants in three-dimensional perspec-

https://doi.org/10.4208/aamm.2014.m829 Published online by Cambridge University Press

tive. Apparently, comparing Fig. 9 and Fig. 8, the time rate of change of the vorticity depends on the competition between vortex stretching and viscous dissipation, and each of them is dominant at different stages during the collision. It is meaningful to separate the whole evolution of the head-on collision of two coaxial vortex rings into three stages: the free-travelling, vortex-stretching, and dominance of viscous dissipation. These are similar to those mentioned in [6].

In the following, we will focus on the vortex rings' variations of helicity, vorticity and kinetic energy during the three stages of the collision prior to the instability appearance.

3.6.2 Free-travelling stage

When a vortex ring is in the free travelling stage, it is the viscous diffusion that causes the decrease of vorticity in the vortex ring. The numerical evidence Fig. 8(a) and Fig. 9(d) confirms this observation.

In the free-travelling stage, the vorticity gradient is zero when r is large. Than the vorticity gradients are small near the z-axis of the vortex ring; thereafter, a slight change of the vorticity magnitude is expected when the vortex rings are some distance apart. Vorticity iso in Fig. 8(f) shows that the trend of the variation of vorticity agrees with the analysis.

3.6.3 Vortex stretching stage

When the vortex rings come close enough, they interact with each other and proceed to vortex stretching. The numerical results show that, during the head-on collision, the vortex ring will increase in size more than 15 times its initial diameter Fig. 9(j). The severe stretching causes a sudden increase of vorticity, which can be seen in the vortex core contours of Fig. 6.

Fig. 9(a) shows that the kinetic energy of a vortex rings $E_{k\text{iso}}$ decays gradually during vortex stretching and the kinetic energy of the whole volume has a sudden reduction. Apparently, the variation of vorticity and kinetic energy depends on the competition between vortex stretching and viscous dissipation. Fig. 9(d) shows that the $\text{vorticity}_{\text{aver}}$ has a sudden increase in the early stage of vortex stretching because of the dominance of the stretching effect. Until the scale of the vortex ring core decreases to a certain limit owing to stretching, the vorticity gradients become so large that the contribution of the viscous dissipation overcomes that of the stretching. Therefore, the vorticity will decrease again, as shown in Fig. 9(h). On the other hand, the sudden increase of the vorticity into the volume during the stretching process will enhance the dissipation of the total kinetic energyaver according to Fig. 9(d). Thus, during vortex stretching, the enhancement of the vortical activity is always accompanied by a speeding up the energy dissipation.

3.6.4 The stage of dominance of viscous dissipation

As shown in Fig. 9(g), when helicity reaches its peak value, the vortex evolution shifts to the stage of dominance of viscous dissipation. From that moment on, the effect of viscous

https://doi.org/10.4208/aamm.2014.m829 Published online by Cambridge University Press

dissipation overcomes that of vortex stretching. However, results from the numerical calculation indicate that flow features associated with the stage of dominance of viscous dissipation, rebound or bulging instability, depend also on the initial separation between vortex rings.

Fig. 9(c) indicates that the vortex ring slows down gradually after it is completely formed while the vortex ring diameter increases gradually because of viscous diffusion. Therefore, the speed changes slightly before the collision. When the vortex rings came together and stretch actively with each other, bulges around the circumference of the vortex rings were observed to appear. This phenomenon is confirmed by [1]. At this moment, the azimuthal component of velocity exists in bulges and the flow is no longer axisymmetric. Fig. 4 shows an example of the bulging instability at various values of time. It is seen in Fig. 2 and Fig. 6 that several bulges were observed to develop around the circumference of the vortex rings when their radii had increased to about four times the initial radius; however, the bulges, continued to grow and then distorted instead of breaking-up towards the end of collision. On the other hand, the flow feature of rebound was observed, as the calculated vorticity centers gradually moved toward each other and eventually rotate from the plane of symmetry during collision, observed in Fig. 5.

3.7 Results summary

The emphasis of Section 3 is placed on the application of the numerical scheme presented early in Section 2. Simulation results of a simple test case are presented: nearly uniform density mixing layer coaxial collision of two vortex rings was observed in three dimensions. Therefore, we present investigations of structure, formation, motion and evolution of the vortex rings. We started with an illustration of the initial setup in Section 3.1 and the essential flow features in Section 3.2 and then examine the behavior of the dynamic model.

The computational setup resembles the experimental conditions of Lim, where striking dye visualizations of these collisions are provided. However, the numerical results also indicate that in some collision events the rings break down into a cloud of turbulence without generating ringlets. This variability and strong dependence on the initial conditions, as well as the development of instabilities, provide a difficult challenge for the computations. Thus, the simulations are used to analyze, qualitatively, possible causes behind the variability between different collision events.

The effects of variables on the evolution of the vortex rings and on the vorticity distribution are investigated by varying, l_z, also as varying V and R of the vortex ring, in the ranges of $6R \leq l_z \leq 12R$, $130 \leq V \leq 230$ and $1.5 \leq l_z \leq 4$. The dynamics of vortex ring evolution are analyzed by means of instantaneous vorticity, pressure contours, and iso-surfaces of the flow.

Meanwhile, simulations are extended into late stages, where severe deformation of the vorticity field, including local cancellation and reconnection are observed. The evolution of the perturbed vortex rings is illustrated in the figures in the Section 3.3. We also

https://doi.org/10.4208/aamm.2014.m829 Published online by Cambridge University Press

provide Section 3.4 with a detailed discussion of the observed phenomenon, evolution of the velocity, kinetic energy, enthalphy, vorticity, helicity together with a brief examination of their physical meaning and deforming phenomena Section 3.5. Furthermore, we present the evolution of the vortex ring as a function of time Section 3.6, and describe the three stages of vortex evolution.

The turbulent eddy viscosity indicates that the vortex rings colliding experience a degree of turbulence during their collision, which then dies off and it appears to last for a short time. The variation of the eddy viscosity is dominated by changes in the vorticity, whose relative variation has much greater range in the whole volume than that in the vorticity iso-surface.

The results show that kinetic energy, vorticity and helicity reveals directly the effects from the vortex stretching and viscous dissipation associated with the three stages of vortex evolution. In the stage offered traveling, the vorticity of a vortex ring decreases owing to viscous dissipation. The early stage of vortex stretching has been shown to be associated with a sudden increase of the total vorticity and a rapid degradation of circulation between two vortex rings while the stage of viscous dissipation dominance is accompanied by a decrease of kinetic energy due to the dominance of viscous dissipation. The analysis also shows that enhancement of the vortical activity of the flow owing to vortex stretching is always accompanied by a speeding up of energy dissipation. The rebound behavior of vortex rings has been observed in the stage of dominance of viscous dissipation and has been found, indeed, to be related to the increase of vorticity core diameter owing to severe viscous dissipation, when the rate of change of helicity reaches a negative minimum with the effect of viscous dissipation predominating that of vortex stretching. The phenomenon of bulging instability around the circumference of a vortex ring has been observed while vortex rings are subjected to stretching during collision. It is found that the occurrence of bulging instability depends on the initial separation of vortex rings, and the initial core-size of the vortex ring. This observation not only enables us to assess the range of validity of the axial symmetry assumed for numerical simulation, but also provides us with a rational basis for further theoretical analysis of azimuthal instability.

The following Section 3.7 is a conclusion of the developed method and his practical application of vortex rings for solving an important technological problem.

Compared with the LES numerical simulation of similar problem of vortex rings collision in reference [15], it can be seen that both of us capture the key features of the problem, and in our results the generation and develop of small-scale radially propagating vortex rings is more clear and reveal more careful of the effect of turbulence to the evolution of vortex structures.

4 Conclusions

The focus of the present study is to examine the effect of the collision on the motion of t-

https://doi.org/10.4208/aamm.2014.m829 Published online by Cambridge University Press

wo vortex rings. Therefore, computational investigations of structure, formation, motion and evolution of the vortex rings were made. Irrespective of the outcome of the collision, the turbulent nature of the interaction between the colliding rings provides a stringent test for the computations. The latter show that the present combination of non-iterative approximate Riemann solver and piecewise-parabolic reconstruction results in a scheme that can capture complex flow dynamics with a reasonable number of elements.

The computations of vortex ring collisions shows that, the used scheme can be extended into the late stages of the evolution of flow and capture several distinctive phenomena that were observed early in laboratory experiments, including the approach and stretching of the rings, strong interaction between the vortex cores with local cancellations and reconnections, the generation of small-scale turbulent structures, and the formation of ringlets propagating radially away from the center of collision. The observations shows that kinetic energy, vorticity and helicity reveals directly the effects from the vortex stretching and viscous dissipation associated with the three stages of vortex evolution (the free-travelling, vortex-stretching, and dominance of viscous dissipation).

In the present application few parameters are obtained by averaging over all the volume and particular iso-surface, thus combining information from different regions of the flow (e.g., highly strained regions around vortex cores and "inactive" regions in the volume corners) to determine a single parameter in space, is an approach that is especially suited for vortex methods.

Based on the present numerical investigation, it is clear that the merge and deformation of the vortex rings, caused by their head-on collision is following by separation and reconnection, due to the modification of the vorticity distribution, as a result of the entrainment of background vorticity and helicity by the vortex core, and their subsequent interaction. In addition, a vorticity gradient is created along the core, which causes further deformation, elongation, and reorientation of new clumps. The new orientation of the separated structures, new formed small vortex ringlets, increases with the increase in the radial distance, and decreases with the decreases in vorticity. The observed phenomenon could be attributed to the modification of vorticity distribution of the core due to the combined effect of the collision itself and the entrainment of boundary layer material during the formation of the ring.

The dynamic implementation of the model concentrates computational elements into regions of high vorticity and minimizes the numerical diffusion. Also for the conditions of the simulations, the dynamic model does not affect the propagation velocity or diameter expansion of the colliding rings prior to reconnection. The variation of the eddy viscosity is dominated by changes in the vorticity, whose relative variation has much greater range in the whole volume than that in the vorticity iso-surface. The turbulent eddy viscosity indicates that the vortex rings colliding experience a degree of turbulence during their collision, which steadily dies off. Due to their natural ability to capture inviscid dynamics of concentrated energetic eddies, second order explicit scheme appear to provide a promising approach to large-eddy-simulation of turbulent flows.

Future efforts must be directed toward achieving a better understanding of the rapid

https://doi.org/10.4208/aamm.2014.m829 Published online by Cambridge University Press

convective entrainment process that occurs during new vortex ringlets formation. One can infer from the present study that this early phase of entrainment will be responsible for much of the entrained fluid fraction that persists in the vortex rings. The current method has definitively shown a substantial contribution of ambient fluid entrainment to the dynamics of vortex rings. As improved vortex ring models are being developed, it will be prudent to account for this phenomenon. The additional work can be used to clearly quantify the effect of the sub-grid scale model. One could extend the computations to model problems where the turbulence is well characterized (forced isotropic turbulence).

These results may have important implications for pulsed jet systems that possess a capability to manipulate the vortex ring velocity and vorticity distribution. Notwithstanding the many manmade applications that may be designed to exploit these parameters in the future, various animals may have already achieved success in this endeavor; it will be interesting to further examine the relationship between vorticity distribution and the effectiveness of entrainment mechanisms in these animals. Nowadays, human body fluids are also considered as attractive sources for vortex rings, which analysis can be useful for health diagnosis and prognosis.

Acknowledgments

The project was supported by the National Natural Science Foundation of China No. 11372068 and the National Key Basic Research and Development Program of China No. 2014CB744104.

References

[1] T. T. LIM AND T. B. NICKELS, *Instability and reconnection in the head-on collision of two vortex rings,* Nature, 357 (1992), pp. 225–227.
[2] AKHMETOV AND D. GAZIZOVICH, Vortex Rings, Springer Science and Business Media, Berlin Heidelberg, 2009.
[3] Y. OSHIMA, *Head-on collision of two vortex rings,* J. Phys. Soc. Japan, 44 (1978), pp. 328–331.
[4] T. KAMBE AND T. MINOTA, *Acoustic wave radiated by head-on collision of two vortex rings,* P. Roy. Soc. A Math. Phy., 386 (1983), pp. 277–308.
[5] T. KAMBE AND U. MYA OO, *An axisymmetric viscous vortex motion and its acoustic emission,* J. Phys. Soc. Japan, 53 (1984), pp. 2263–2273.
[6] C. CHU, C. WANG, C. CHANG, R. CHANG AND W. CHANG, *Head-on collision of two coaxial vortex rings: experiment and computation,* J. Fluid Mech., 296 (1995), pp. 39–71.
[7] A. J. CHORIN, *Hairpin removal in vortex interactions,* J. Comput. Phys., 91 (1990), pp. 1–21.
[8] A. J. CHORIN, Vorticity and Turbulence, Springer Science and Business Media, 1994.
[9] P. S. BERNARD, *A vortex method for wall bounded turbulent flows*, EDP Sci., (1996), pp. 15–31.
[10] J. C. SAGHBINI, Simulation of Vorticity Dynamics in Swirling Flows, Mixing and Vortex Breakdown, PH.D thesis, 1996.

https://doi.org/10.4208/aamm.2014.m829 Published online by Cambridge University Press

[11] V. M. FERNANDEZ, N. J. ZABUSKY, P. LIU, S. BHATT AND A. GERASOULIS, *Filament surgery and temporal grid adaptivity extensions to a parallel tree code for simulation and diagnosis in 3D vortex dynamics,* EDP Sci., (1996), pp. 197–211.
[12] A. J. CHORIN AND O. H. HALD, *Vortex renormalization in three space dimensions,* Phys. Rev. B, 51 (1995), pp. 11–969.
[13] A. J. CHORIN, *Microstructure, renormalization, and more efficient vortex methods,* EDP Sci., (1996), pp. 1–14.
[14] A. J. CHORIN AND O. H. HALD, *Analysis of Kosterlitz-Thouless transition models,* Phys. D Nonlinear Phenomena, 99 (1997), pp. 442–470.
[15] J. R. MANSFIELD, O. M. KNIO AND C. MENEVEAU, *Dynamic LES of colliding vortex rings using a 3D vortex method,* J. Comput. Phys., 152 (1999), pp. 305–345.
[16] T. T. BUI, *A parallel, finite-volume algorithm for large-eddy simulation of turbulent flows,* Comput. Fluids, 29 (2000), pp. 877–915.
[17] B. VREMAN, B. GEURTS AND H. KUERTEN, *Subgrid modeling in LES of compressible flow*, Appl. Sci. Res., 51 (1995), pp. 191–203.
[18] A. A. CHERNOUSOV, *LES of mixing layer and flow in square duct by the second-order explicit scheme,* (2001).
[19] J. SMAGORINSKY, *General circulation experiments with the primitive equations: I. the basic experiment,* Mon. Weather Rev., 91 (1963), pp. 99–164.
[20] S. R. CHAKRAVARTHY AND S. OSHER, *A new class of high accuracy TVD schemes for hyperbolic conservation laws,* AIAA Paper No. 85-0363 (1985).
[21] A. A. CHERNOUSOV, *A characteristic-based approximate Riemann solver,* Technical report, Ufa State Aviation Technical University, (2001).
[22] S. GOTTLIEB AND C. SHU, *Total variation diminishing Runge-Kutta schemes,* Math. Comput. American Math. Society, 67 (1998), pp. 73–85.
[23] Z. JACKIEWICZ, R. RENAUT AND A. FELDSTEIN, *Two-step Runge-Kutta methods,* SIAM J. Numer. Anal., 28 (1991), pp. 1165–1182.
[24] G. L. BROWN AND A. ROSHKO, *On density effects and large structure in turbulent mixing layers,* J. Fluid Mech., 64 (1974), pp. 775–816.
[25] S. MENON AND J. H. SOO, *Simulation of vortex dynamics in three-dimensional synthetic and free jets using the large-eddy lattice Boltzmann method,* J. Turbul., 5 (2004), pp. 1–4.
[26] O. REYNOLDS, *On the resistance encountered by vortex rings and the relation between vortex rings and the stream-lines of a disc,* Nature, 14 (1876), pp. 477–479.
[27] T. MAXWORTHY, *The structure and stability of vortex rings*, J. Fluid Mech, 51 (1972), pp. 15–32.
[28] O. M. KNIO AND A. F. GHONIEM, *Numerical study of a three-dimensional vortex method,* J. Comput. Phys., 86 (1990), pp. 75–106.
[29] S. E. WIDNALL AND C. TSAI, *The instability of the thin vortex ring of constant vorticity,* Philosophical Transactions of the Royal Society of London. Series A, Mathematical and Physical Sciences, 287(1977), 273-305.
[30] C. SHU AND S. OSHER, *Efficient implementation of essentially non-oscillatory shock-capturing schemes,* J. Comput. Phys., 77 (1988), pp. 439–471.
[31] B. COCKBURN AND C. SHU, *TVB Runge-Kutta local projection discontinuous Galerkin finite element method for conservation laws. II. General framework,* Math. Comput., 52 (1989), pp. 411–435.
[32] A. HARTEN, *High resolution schemes for hyperbolic conservation laws,* J. Comput. Phys., 49 (1983), pp. 357–393.
[33] S. OSHER AND S. CHAKRAVARTHY, *High resolution schemes and the entropy condition,* SIAM J.

https://doi.org/10.4208/aamm.2014.m829 Published online by Cambridge University Press

Numer. Anal., 21 (1984), pp. 955–984.
[34] P. K. SWEBY, *High resolution schemes using flux limiters for hyperbolic conservation laws*, SIAM J. Numer. Anal., 21 (1984), pp. 995–1011.
[35] C. SHU, *TVB uniformly high-order schemes for conservation laws,* Math. Comput., 49 (1987), pp. 105–121.
[36] A. HARTEN, B. ENGQUIST, S. OSHER AND S. R. CHAKRAVARTHY, *Uniformly high order accurate essentially non-oscillatory schemes, III,* J. Comput. Phys., 71 (1987), pp. 231–303.
[37] B. COCKBURN, S. HOU AND C. SHU, *The Runge-Kutta local projection discontinuous Galerkin finite element method for conservation laws. IV, The multidimensional case,* Math. Comput., 54 (1990), pp. 545–581.
[38] J. H. WILLIAMSON, *Low-storage Runge-Kutta schemes*, J. Comput. Phys., 35 (1980), pp. 48–56.
[39] M. H. CARPENTER AND C. A. KENNEDY, *Fourth-order 2N-storage Runge-Kutta schemes,* NASA Langley Research Center, (1994).
[40] B. VAN LEER, *Towards the ultimate conservative difference scheme V. A second-order sequel to Godunov's method,* J. Comput. Phys., 32 (1979), pp. 101–136.

https://doi.org/10.4208/aamm.2014.m829 Published online by Cambridge University Press